Catalyzed Growth of Carbon Nanotube with Definable Chirality by Hybrid Molecular Dynamics—Force Biased Monte Carlo Simulations

Erik C. Neyts,[†,]* Yasushi Shibuta,[‡] Adri C. T. van Duin,[§] and Annemie Bogaerts[†]

[†]Department of Chemistry, University of Antwerp, Research group PLASMANT, Universiteitsplein 1, 2610 Antwerp, Belgium, [‡]Department of Materials Engineering, The University of Tokyo, 7-3-1 Hongo, Bunkyo-Ku, Tokyo 113-8656, Japan, and [§]Department of Mechanical and Nuclear Engineering, Penn State University, University Park, Pennsylvania 16801, United States

ABSTRACT Metal-catalyzed growth mechanisms of carbon nanotubes (CNTs) were studied by hybrid molecular dynamics—Monte Carlo simulations using a recently developed ReaxFF reactive force field. Using this novel approach, including relaxation effects, a CNT with definable chirality is obtained, and a step-by-step atomistic description of the nucleation process is presented. Both root and tip growth mechanisms are observed. The importance of the relaxation of the network is highlighted by the observed healing of defects.

KEYWORDS: SWNT nucleation mechanism · hybrid MD/UFMC simulations · ReaxFF reactive force field · chirality · defect healing

Since their first preparation in 1993,[1] single-walled carbon nanotubes (SWCNTs) have been intensively studied because of their extraordinary mechanical, optical, and electronical properties.[2,3] These properties make them excellent candidates for application in numerous fields, including microelectronics, medical applications, and materials science.[4] These applications, however, depend to a large extent on our ability to control their growth and thereby their structure. Indeed, the electronic properties of SWCNTs are primarily determined by their chirality, as this determines whether the tube is metallic or semiconducting, as well as its band gap. At present, the controlled growth of SWCNTs with a predefined chirality has not yet been achieved, due to an incomplete understanding of their growth mechanism on the atomic level. The most promising way of producing SWCNTs with predefined chirality is catalytic chemical vapor deposition (CCVD).[5,6] Here, a hydrocarbon gas (such as CH_4, C_2H_2, etc.) is catalytically decomposed on a metal nanoparticle (Ni, Fe, Co, FeMo, etc.) into atomic carbon.[7−9]

Currently, two qualitative models for CCVD growth are proposed. In the vapor−liquid−solid model (VLS),[10] the catalyst particle is in the liquid state, which allows rapid diffusion of carbon atoms throughout the particle. Another mechanism, the surface-mediated carbon transport model, has been proposed to explain the low temperature nanotube growth by plasma enhanced CVD (PECVD).[11,12]

Two growth modes can be distinguished: root growth and tip growth. In root growth, the catalyst particle stays pinned at the support surface, whereas tip-growth takes place when the catalyst is lifted off from the support surface during CNT growth due to weak support-catalyst interaction.[13] The term tip growth is also used to denote the process in which additional carbon atoms are added to the CNT by the catalytic action of single metal atoms incorporated in the tip of the CNT.[14]

Various authors have investigated the growth of SWCNTs by classical molecular dynamics (MD) to gain insight in the growth mechanism.[15−23] Shibuta et al. investigated the nucleation process of SWCNTs, both for a laser ablation growth process,[15] as well as for CCVD, thereby focusing on the effect of pressure and nanocatalyst particle size.[16] These studies demonstrated the use of classical MD in revealing atomistic details during the catalytic growth of SWNTs. It was determined how the local shape of the catalyst surface controls cap lift-off from the catalyst surface. Ding et al. studied the influence of temperature and catalyst particle size on the growth.[17−19] The growth mechanism was found to shift from bulk diffusion mediated to surface diffusion mediated at around 900−1000 K. Also, it was concluded
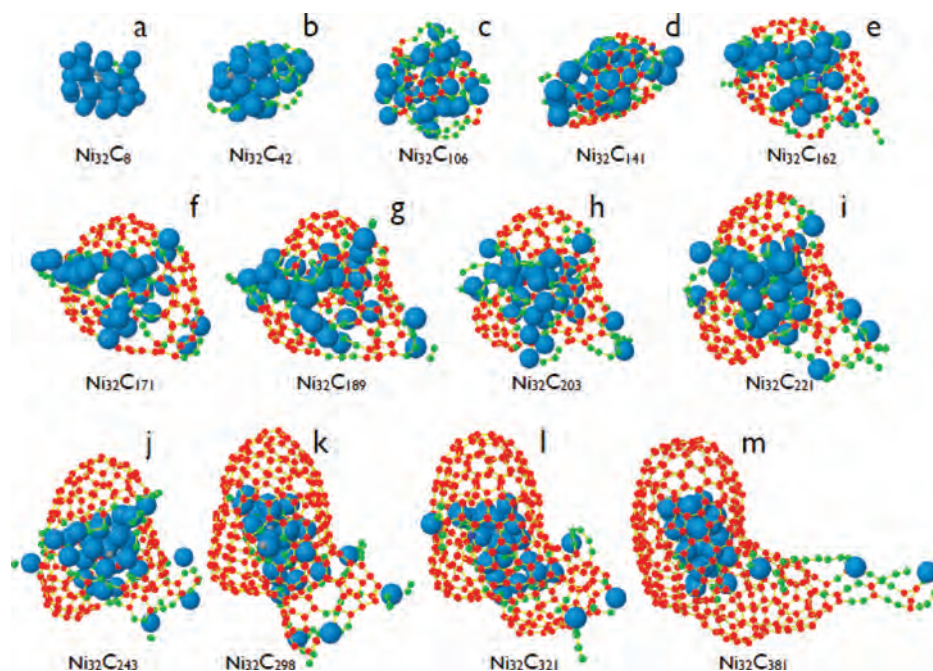
Figure 1. Step-by-step evolution of the SWNT growth process. The carbon atoms are color coded accoring to C−C coordination: green = 2-coordinated; red = 3-coordinated; dark blue = 4-coordinated. The light blue big spheres represent Ni atoms.

that while a temperature gradient may be important for larger particles, it is not required for SWNT growth from small particles. Ding *et al.* also studied the influence of the structure and thermal properties of the nanocatalyst,[20] demonstrating the increase in melting temperature for clusters strongly interacting with the substrate, important for surface bound CNT growth. Zhao *et al.* also investigated SWCNT cap formation focusing on the nanoparticle size,[21] stressing the importance of the formation of an (nearly) ideal stable cap and the healing of defects. Recently, Ribas *et al.* and Burgos *et al.* performed elaborate MD simulations investigating the growth of SWNTs focusing on the interaction between the metal cluster and the carbon network.[22,23] It was concluded that for a given temperature, both the work of adhesion between the graphitic cap and the catalyst and the size of the catalyst are decisive factors in controlling catalyst poisoning or growth.

Also quantum mechanical MD studies have been performed to simulate the growth of SWNTs, focusing mainly on the initial nucleation stage.[24−27]

However, all of these simulations employ a carbon addition rate to the nanocatalyst in the order of 1 atom per 50 ps (or faster), and hence do not include relaxation effects. This addition rate is more than 4 orders of magnitude too high compared to the experiment (based on a growth rate[28] of about 20 μm/s). As a result, none of these simulations have succeeded in the growth of structures with a defined chirality. Indeed, the much lower carbon addition rate in the experiment allows relaxation processes to occur. However, calculations by classical MD would take a prohibitively long calculation time if a realistic carbon addition rate were

to be applied. To extend the time scale of MD simulations, in order to include relaxation processes, so-called accelerated MD simulations (such as hyperdynamics, parallel replica, or temperature accelerated dynamics) can be applied.[29] However, we have recently shown that the fundamental dynamics in the carbon−nickel system at SWCNT growth temperatures are too fast to apply accelerated MD techniques.[30]

Alternatively, deterministic MD simulations can be coupled to stochastic MC simulations, for instance uniform-acceptance force biased Monte Carlo (UFMC) allowing to take into account relaxation effects,[31−33] albeit at the price of loosing time information. Recently, we have successfully applied a hybrid MD/UFMC approach for the simulation of the melting mechanisms of nickel nanoclusters.[28] In this work, we propose this novel methodology to simulate SWNT nucleation taking into account relaxation processes. It is demonstrated that taking into account these relaxation processes is required in order to obtain a SWNT cap. The growth process is shown to proceed through various stages which are analyzed on the atomic level. Finally, various metal-mediated defect healing processes are observed, leading to the formation of a SWNT cap with definable (12,4) chirality.

RESULTS AND DISCUSSION

The simulations demonstrate the following eight stages in the nucleation of a SWNT, as is illustrated in Figure 1.

Alloying Stage. In the first stage, impinging gas phase carbon atoms easily adsorb on the surface of the cluster and subsequently dissolve into the nickel cluster,
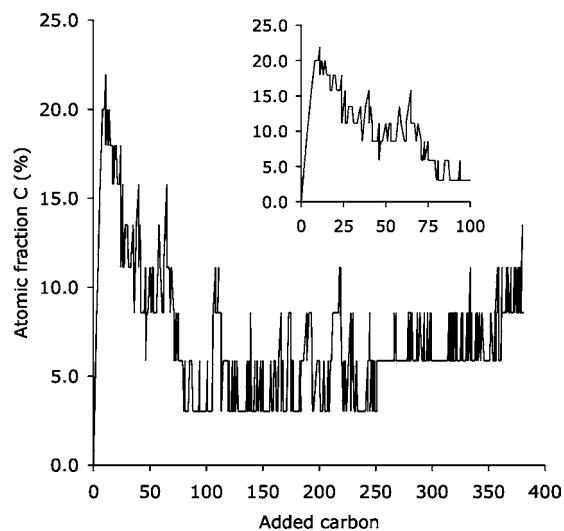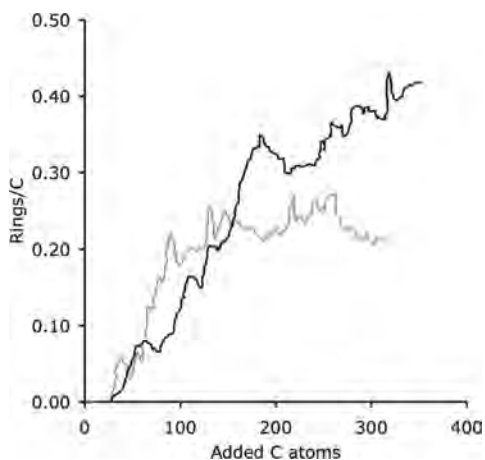
Figure 2. Atomic carbon percent in the metal cluster as a function of the number of incorporated carbon atoms. The inset shows a magnified view of the initial alloying stage, supersaturation point, and subsequent decrease in atomic carbon content in the cluster.

Figure 3. Number of rings (summed over pentagons, hexagons, and heptagons) per incorporated carbon atom as a function of the number of added carbon atoms. The black line corresponds to the MD/UFMC simulation, while the gray line corresponds to the pure MD simulation.

where they preferentially occupy subsurface sites. They diffuse very quickly in the surface/subsurface region, appearing at the surface and dissolving in the subsurface region again. Occasionally, carbon atoms move into the bulk of the cluster (*i.e.*, beyond the subsurface layer), but quickly return to the subsurface and surface regions. In this stage, the carbon atoms do not form bonds, but tend to move away from other carbon atoms as far as possible, thereby forming a carbon/nickel alloy. At this point, the atomic carbon fraction in the cluster is about 22%, corresponding to the addition of 9 carbon atoms to the cluster (see maximum in Figure 2), corresponding to the supersaturation point.

Saturation/Supersaturation Stage. This process continues until there is no room left for additional carbon atoms to be added without forming C—C bonds. There is, however, still plenty of room at the metal surface to "catalyze" the dissociation of hydrocarbon molecules into carbon atoms, and hence to further increase the carbon content in the cluster and at the cluster surface. At this point, the dissolved carbon starts to form C—C bonds (see Figure 1a) in the form of dimers, thereby causing a drop in the fraction of atomic carbon. Dimers form both from carbon atoms added from the gas phase after the supersaturation point as well as from pairs of carbon atoms added to the cluster in the initial alloying stage. The continued addition of carbon leads to the formation of trimers. Both the dimers and trimers exist both on the surface and in the subsurface region. Longer chains containing more than three carbon atoms, however, appear only at the surface.

Initial Ring Formation. Owing to the continued addition of carbon, the first rings start to appear (Figure 1b).[24] These first rings do not form by coalescence of dimers, trimers, or longer chains, but rather from rear-

ranging short single chains and the subsequent addition of carbon atoms. For instance, a trimer may rearrange into a (short-lived) triangle, to which carbon atoms may add leading to the formation of a square, a pentagon, and finally a hexagon. While trimers and squares are not very stable, their occurrence provides a pathway to the formation of stable larger rings. Alternatively, short chains of five or six atoms may also rearrange directly into a pentagon or a hexagon, respectively. The added carbon atoms are found to originate both from the gas phase impinging in the vicinity of the ring, as well as from diffusing surface and subsurface carbon atoms. During this stage, the fraction of single carbon atoms drops to about 10% (see Figure 2).

Ring Formation of the Second Generation. After the formation of these first rings, long surface chains containing eight or more carbon atoms start to appear on the surface due to the continued addition of carbon from the gas phase and from single carbon atoms in the subsurface region of the cluster. Because of the continuous reshaping of these long chains, parts of these chains may connect to each other and rings of the second generation are formed, ranging from triangles with long tails to octagons (Figure 1c). During this stage, the fraction of single carbon atoms drops to about 5% (see Figure 2). Also during this stage, the first concatenated ring systems are found, forming the initial nuclei, which will grow into graphitic islands in a later stage (see later). The evolution of the number of rings (counted as the sum of pentagons, hexagons, and heptagons) per incorporated carbon atom is shown in Figure 3 (black line), demonstrating the growth of the graphitic network as a function of the number of incorporated carbon atoms.

Graphitic Island Formation. Concatenated rings are not formed by coalescence of single rings, but rather from the addition of single carbon atoms, dimers, and trimers to existing rings, forming short tails. These tails pref-
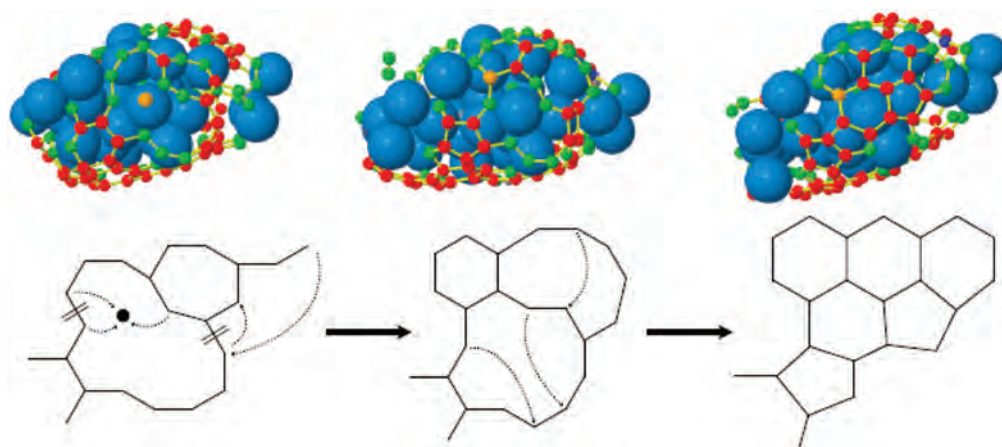
Figure 4. Detailed mechanism showing the formation of larger graphitic islands from long chains by the addition of a single gas phase carbon atom using the same color coding as Figure 1. The orange atom in the left Figure is the carbon atom in the gas phase that is subsequently added to the cluster, inducing a cascade of bond rearrangements. The dashed lines in the schematic representations indicate the formation of new C−C bonds, while the short double lines indicate the breaking of C−C bonds.

erentially adopt valence angles around 120°, and therefore preferentially form pentagons and hexagons by the subsequent addition of single carbon atoms (Figure 1d). This ring growth mechanism—addition of monomers, dimers, and trimers to rings forming surface tails leading to ring formation—generates the first graphitic islands. Several small graphitic islands, each consisting of three or four rings, are found to coexist at the surface. During this stage, the fraction of atomic carbon in the cluster oscillates between 3 and 8% (see Figure 2).

It should be noted that at this temperature, the Ni-atoms of a nanocluster of this size are highly mobile,[30,33] and do not provide a template for the carbon ring formation. Further, the formation of the graphitic islands induces a dynamic reshaping of the nickel cluster to an ellipsoidal shape: Indeed, as the graphitic islands are still very small in this stage, the high curvature energy prevents them from curving around a spherical cluster, and therefore they tend to flatten the nickel cluster (see Figure 1d).

Coalescence of Graphitic Islands. The small graphitic islands are connected to each other by the long surface chains. These chains, consisting of sp-bonded carbon, are highly flexible, and the introduction of a single atom may lead to a cascade of bond reorganizations in the chains, thereby forming a new graphitic island, connecting the islands to which the chains were connected. This process is illustrated in detail in Figure 4. Thus, this leads to the formation of large graphitic islands, spanning a considerable fraction of the surface area of the cluster. At this point, the graphitic islands are big enough to follow the curvature of the metal cluster, and the metal cluster becomes somewhat more spherical again (albeit still ellipsoidal). In this reshaping process, however, some Ni atoms detach from the metal cluster, and remain attached to the Ni/C cluster by Ni−C bonds

only. These detached metal atoms will be responsible for a tip growth mechanism in a later stage (see later).

Cap and Tube Formation by Root Growth. The large graphitic islands are connected to the metal cluster by the carbon atoms at the edge of the islands (Figure 1e). As new carbon atoms are incorporated in the growing network at the edge of the islands (either from gas phase atoms or from previously dissolved atoms), these edge atoms are continuously being replaced by new atoms, and the graphitic island is lifted off from the surface of the metal cluster (Figure 1f). Therefore, the "oldest" atoms are those in the center of the cap (forming the "tube closure"), while the newest atoms are those closest to the metal, corresponding to a root growth mechanism (see Figure S1 in the Supporting Information). Initially, the cap is not spherical at all, but closely resembles the curvature shape of the metal cluster area from where the cap is lifted off. As more carbon is incorporated in the network, the cap becomes a hemisphere and a vertical tube emerges (Figure 1g−l). In this particular case two fairly large graphitic islands coexist, and two caps are formed as can be seen in Figure 1i. However, the continued addition of carbon to the metal cluster ultimately leads to coalescence of both caps (Figure 1l). Note that the atomic carbon content in the cluster increases slightly to about 10% (see Figure 2).

Tube Formation by Tip Growth. As mentioned above, in the formation process of the large graphitic islands, the metal cluster is reshaped according to the curvature of the carbon network. In this process, some Ni atoms detach from the rest of the metal cluster (Figure 1e). These lone Ni atoms may also catalyze gas phase carbon atoms to be incorporated in the network. Carbon atoms added to the network from these detached metal atoms initially form long chains and large rings (Figure 1i). These chains and rings are highly flexible and can easily connect to each other, thereby forming pentagons, hexagons, and heptagons with linear tails,

a

b

c

$C_{gasphase}$
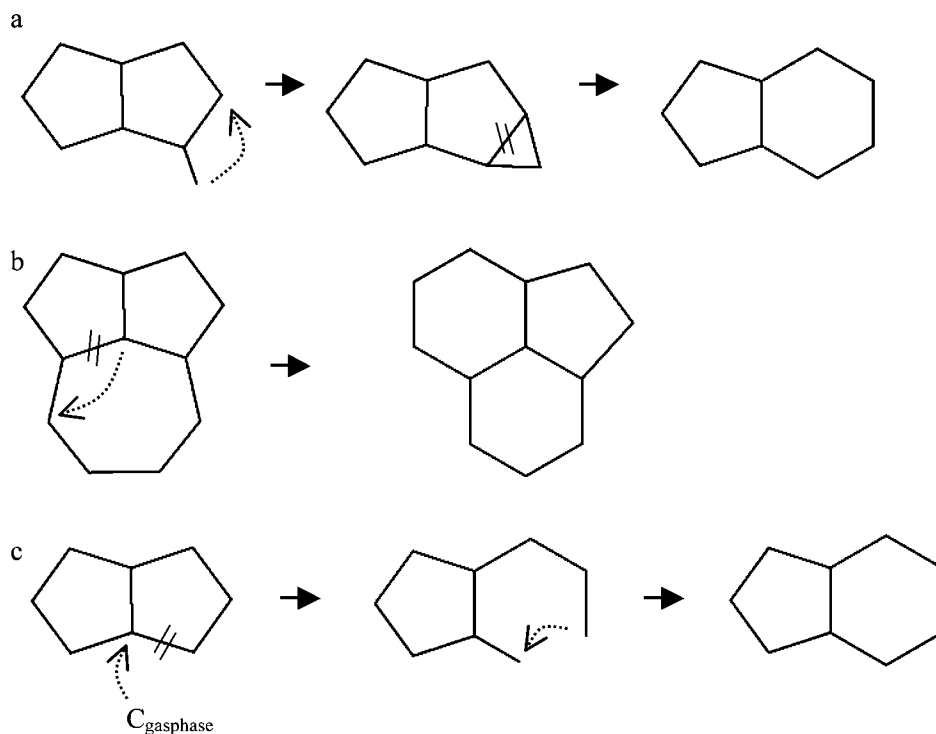
Figure 5. Mechanisms of metal mediated defect healing during relaxation of the carbon network; (a) pentagon to hexagon transformation over a pentagon/triangle intermediate; (b) transformation of a pentagon/heptagon structure to two hexagons by simple bond switching; (c) transformation of a pentagon into a hexagon initiated by incorporation of a gas phase carbon atom and subsequent relaxation.

resulting in the formation of a (defective) curved graphene sheet (see arrow in Figure 1j−l). The metal atoms move around near the edges of the sheet, allowing for the continued addition of gas phase carbon atoms with the formation of new chains. When the graphene sheets become large enough, the chains provide a flexible framework for the sheet to curve into a tube (Figure 1m). The metal atoms remain near the tip of the tube, allowing the incorporation of new carbon atoms into the network. This therefore corresponds to a tip growth mechanism. It is possible, however, that the detached metal atoms might lead to instability during further growth of the tube. Simulating the continued growth is, however, beyond the scope of this study because of calculation time limitations.

Effect of the Relaxation of the Carbon Network. The effect of relaxing the network is demonstrated by the observed metal-mediated healing of nonhexagonal defects. In Figure 5, three mechanisms are shown which are observed to transform pentagons and heptagons (*i.e.*, defects) into hexagons. In the first mechanism (Figure 5a), a carbon atom connected to a pentagon connects to an adjacent carbon atom forming a triangle. Because of the ring strain, this triangle is unstable and the bond separating the triangle from the pentagon is broken, thereby forming a hexagon. In the second mechanism (Figure 5b), a pentagon/heptagon structure is transformed into two hexagons by simple bond switching. The third mechanism (Figure 5c) is initiated by the electrophilic attack of a gas phase carbon atom at a car-

bon atom connecting two pentagons. One of the pentagons subsequently opens up and forms a hexagon in the following relaxation stage. Our simulations indicate that all of these three mechanisms are metal-mediated, that is, they only occur when the carbon network is still connected to the metal (*i.e.*, before cap lift-off).

To check the stability of a typical CNT defect after cap lift-off, we have calculated the uncatalyzed energy barrier for the 5775 Stone−Wales defect. We obtain a value of about 8.9 eV for the defect formation (upper boundary), which is close to the *ab initio* value of 8.6 eV reported by Zhao *et al.*[34] and the tight-binding value of 8.5 eV reported by Zhang *et al.*[35] The energy barrier for the uncatalyzed back reaction is calculated to be 6.0 eV (upper boundary), close to the tight-binding value[35] of 5.5 eV. This indicates that this defect is indeed metastable at the growth temperature and is not likely to be healed after cap lift-off.

As a consequence of the defect healing, an elongated cap is formed with relatively few defects, allowing the determination of (*n,m*) indices. The diameter of the cap is $D = 11.45$ Å and the chiral angle $\theta = 14°$ (see Figure 6). From the fundamental relations[36]

$$\theta = \tan^{-1}\left(\frac{\sqrt{3}m}{2n + m}\right)$$
$$D = \frac{a}{\pi}\sqrt{n^2 + nm + m^2}$$

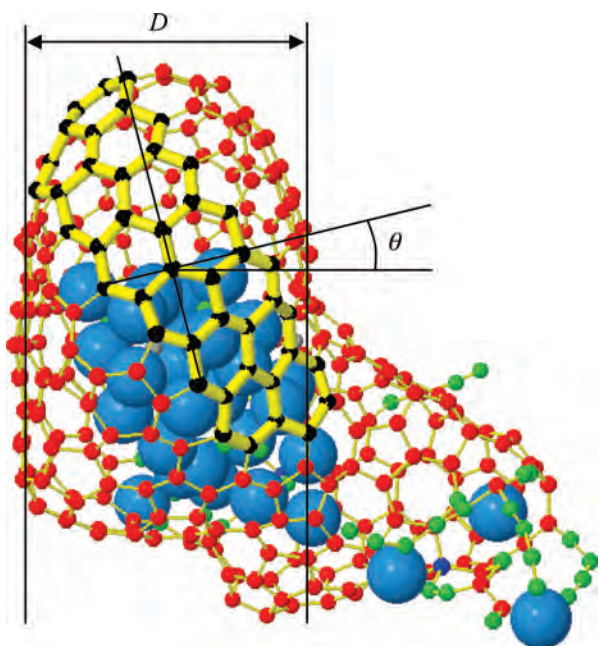where *a* is the lattice parameter of graphene, we find

Figure 6. Determination of chiral angle θ = 14° and diameter D = 11.45 Å of the resulting CNT cap structure, corresponding to a (12,4) chirality.

the chirality of the cap to correspond to a (12,4) CNT. We are currently pursuing simulations to test if other chiralities can be obtained by modifying the growth conditions.

Comparing the growth process emerging from the hybrid MD/UFMC simulation (as described above) to a pure MD simulation highlights the importance of taking into account relaxation effects in the simulation. Indeed, in pure MD simulations, the high carbon addition rate (every 2 ps) is not moderated by the relax-

ation effects between two impacts, leading to the formation of an amorphous, mostly sp[2] bonded carbon network, without the formation of any tube-like or cap-like features (see Figure S2 in the Supporting Information). Rather, long linear chains are formed that are attached to the catalyst on one side and freely floating in vacuum on the other side.[37] Failure to form a growing cap/tube is also apparent from the stagnating number of rings per added carbon atom (see Figure 3, gray line). Finally, it is also observed that far more metal atoms detach from the metal cluster due to the formation of the graphitic network.

SUMMARY AND CONCLUSIONS

We have presented a novel way to simulate the growth process of SWNTs taking into account relaxation effects by coupling deterministic MD simulations to stochastic UFMC simulations. We have shown how the nucleation process proceeds by the initial formation of dimers, trimers, and short chains followed by the formation of the first rings, which corresponds also to *ab initio* calculations.[24] Graphitic islands originate from the presence of long surface chains, which subsequently coalesce into large islands that develop into small SWNT caps. Continued addition of carbon to the metal cluster leads to tube growth by a root growth mechanism. Furthermore, it is shown how metal atoms may detach from the rest of the metal cluster during the graphitic island formation, leading to a tip growth mechanism. Including relaxation effects in the simulation allows for metal mediated healing of defects, leading to a relatively defect free cap structure with (12,4) chirality.

METHODS

Our simulations are based on the Reax Force Field (ReaxFF).[38,39] ReaxFF uses the bond order/bond distance relationship formally introduced by Abel,[40] and applied to carbon by Tersoff[41] and to hydrocarbons by Brenner[42] to describe carbon chemistry. Bond orders, summed from σ, π, and ππ contributions, are calculated instantaneously from interatomic distances.

$$BO_{ij} = BO_{ij}^{\sigma} + BO_{ij}^{\pi} + BO_{ij}^{\pi\pi} = \exp\left[p_{bo1}\left(\frac{r_{ij}}{r_0^{\sigma}}\right)^{p_{bo2}}\right] + \exp\left[p_{bo3}\left(\frac{r_{ij}}{r_0^{\pi}}\right)^{p_{bo4}}\right] + \exp\left[p_{bo5}\left(\frac{r_{ij}}{r_0^{\pi\pi}}\right)^{p_{bo6}}\right]$$

where r_{ij} is the scalar distance between atoms i and j, r_0 equilibrium distances, and p_{bo1} to p_{bo6} are fitting parameters. Overcoordination and undercoordination energy penalties are then used to enforce the correct bond order. The total system energy is a sum of several partial energy terms; these include energies related to lone pairs, undercoordination, overcoordination, valence and torsion angles, conjugation, and hydrogen bonding, as well as van der Waals and Coulomb interactions. Thus, the total energy can be expressed as

$$E_{system} = E_{bond} + E_{lp} + E_{over} + E_{under} + E_{val} + E_{pen} + E_{coa} + E_{C2} + E_{tors} + E_{H-bond} + E_{vdWaals} + E_{Coulomb} + E_{lj}$$

Because Coulomb and van der Waals interactions are calculated between every pair of atoms, ReaxFF describes not only covalent bonds but also ionic bonds and the whole range of intermediate interactions. Charge distributions are calculated based on geometry and connectivity using the electronegativity equalization method (EEM).[43] The force field parameters were optimized to QM data using a single-parameter search optimization technique as descibed previously.[44] A detailed description of the force field development for the Ni/C system was recently published.[39] Currently, ReaxFF is capable of describing nearly half of the periodic table of the elements and their compounds, including hydrocarbons, silicon/silicon oxide, metals, metal oxides, and metal hydrides. Furthermore, ReaxFF has proved useful in studying a variety of complex chemical systems such as bioapplications, see, for example, refs 39, 45, 46 and references therein.

To prevent the direct addition of gas phase carbon to the carbon network growing on the catalyst surface, a standard repulsive Lennard-Jones (LJ) potential is added to ReaxFF. The LJ potential is only operative between carbon atoms belonging to different clusters or molecules, thus allowing the addition of carbon to the metal surface. This procedure therefore simulates the instantaneous catalysis of hydrocarbons at the catalyst surface.[16,22]

In our hybrid MD/UFMC simulation, MD and UFMC stages are alternating, each providing the input structure for the next stage. Thus, the system is allowed to evolve deterministically using MD for a preset number of steps. The resulting structure is

used as input in the (stochastic) UFMC simulation stage in which the structure is allowed to relax. Then, the relaxed structure is used as input for the next MD stage, and so on. Each MD stage runs for 4 ps using a time step of 0.25 fs employing a velocity Verlet integration scheme. Temperature is controlled at 1200 K using the Berendsen thermostat with a coupling constant of 100 fs. The metal catalyst consists of a prethermalized Ni_{32} nanocluster. Although this size is rather small, it is sufficient to identify all essential processes, and it significantly reduces the required computational time. The final configuration contains more than 400 atoms ($Ni_{32}C_{381}$). Note that the complexity of ReaxFF and the coupling to the MC calculation limit the size of the system that can be handled in a reasonable time. The calculation of a single cap growth process currently takes typically several months on a single processor. New developments in parallel ReaxFF will facilitate future applications to larger systems.[47,48]

Growth is accomplished by adding new gas phase carbon atoms randomly to the simulaton box every 2 ps during the MD stage with velocity components taken from a Maxwellian distribution. Subsequently, the gas phase carbon atoms move through the simulation box until they impinge on the metal cluster. In the UFMC simulation stage the structure is allowed to relax for 10^4 steps at a MC temperature of 1200 K. The maximum displacement of the carbon atoms in the UFMC algorithm is set to 0.1 Å in each Cartesian coordinate. During the UFMC stage, no new gas phase carbon atoms are added to the system.

Note that the carbon addition rate corresponds to a MD pressure that is in fact much too high to obtain SWNT growth (as demonstrated). However, in the current simulation setup, this MD pressure does not correspond to the actual simulation growth pressure, since relaxation is taken into account by means of the UFMC stage during which no carbon atoms are added.

Supporting Information Available: Final structure with the carbon atoms color coded according to their age and structure obtained from pure MD simulations, that is, without UFMC taking into account relaxation of the network. This material is available free of charge *via* the Internet at http://pubs.acs.org.

REFERENCES AND NOTES

1. Iijima, S.; Ichihashi, T. Single-Shell Carbon Nanotubes of 1-nm Diameter. *Nature* **1993**, *363*, 603–605.
2. Saito, R.; Dresselhaus, G.; Dresselhaus, M. S. *In: Physical Properties of Carbon Nanotubes*; Imperial College Press: London, 1998.
3. Sazonova, V.; Yaish, Y.; Üstünel, H.; Roundy, D.; Arias, T.; McEuen, P. L. A Tunable Carbon Nanotube Electromechanical Oscillator. *Nature* **2004**, *431*, 284–287.
4. Baughman, R. H; Zakhidov, A. A.; de Heer, W. A. Carbon Nanotubes—The Route towards Applications. *Science* **2002**, *297*, 787–792.
5. Yazyev, O. V.; Pasquarello, A. Effect of Metal Elements in Catalytic Growth of Carbon Nanotubes. *Phys. Rev. Lett.* **2008**, *100*, 156102.
6. Zhu, H.; Suenaga, K.; Wei, J.; Wang, K.; Wu, D. A Strategy to Control the Chirality of Single-Walled Carbon Nanotubes. *J. Cryst. Growth* **2008**, *310*, 5473–5476.
7. Kong, J.; Soh, H. T.; Cassel, A. M.; Quate, C. F.; Dai, H. J. Synthesis of Individual Single-Walled Carbon Nanotubes on Patterned Silicon Wafers. *Nature* **1998**, *395*, 878–881.
8. Geohegan, D. B.; Puretzky, A. A.; Ivanov, I. N.; Jesse, S.; Eres, G.; Howe, J. Y. *In Situ* Growth Rate Measurements and Length Control during Chemical Vapor Deposition of Vertically Allligned Multiwall Carbon Nanotubes. *Appl. Phys. Lett.* **2003**, *93*, 1851–1853.
9. Harutyunyan, A. R.; Pradhan, B. K.; Kim, U. J.; Chen, G. G.; Eklund, P. C. CVD Synthesis of Single Wall Carbon Nanotubes under "Soft" Conditions. *Nano Lett.* **2002**, *2*, 525–530.
10. Wagner, R. S.; Ellis, W. C. Vapor–Liquid–Solid Mechanism of Single Crystal Growth. *Appl. Phys. Lett.* **1964**, *4*, 89–90.
11. Helveg, S.; Lopez-Cartes, C.; Sehested, J.; Hansen, P. L.; Clausen, B. S.; Rostrup-Nielsen, J. R.; Abild-Pedersen, F.; Norskov, J. K. Atomic-Scale Imaging of Carbon Nanofibre Growth. *Nature* **2004**, *427*, 426–429.
12. Abild-Pedersen, F.; Norskov, J. K.; Rostrup-Nielsen, J. R.; Sehested, J.; Helveg, S. Mechanisms for Catalytic Carbon Nanofibre Growth Studied by *ab Initio* Density Functional Theory Calculations. *Phys. Rev. B* **2006**, *73*, 115419.
13. Moisala, A.; Nasibulin, A. G.; Kauppinen, E. I. The Role of Metal Nanoparticles in the Catalytic Production of Single-Walled Carbon Nanotubes—A Review. *J. Phys.: Condens. Matter* **2003**, *15*, S3011–S3035.
14. Charlier, J.-C.; Amara, H.; Lambin, Ph. Catalytically Assisted Tip Growth Mechanism for Single-Wall Carbon Nanotubes. *ACS Nano* **2007**, *1*, 202–207.
15. Shibuta, Y.; Maruyama, S. Molecular Dynamics Simulation of Generation Process of SWNTs. *Phys. B* **2002**, *323*, 187–189.
16. Shibuta, Y.; Maruyama, S. Molecular Dynamics Simulation of Formation Process of Single-Walled Carbon Nanotubes by CCVD Method. *Chem. Phys. Lett.* **2003**, *382*, 381–386.
17. Ding, F.; Rosén, A.; Bolton, K. Dependence of SWNT Growth Mechanism on Temperature and Catalyst Particle Size: Bulk *versus* Surface Diffusion. *Carbon* **2005**, *43*, 2215–2217.
18. Ding, F.; Rosén, A.; Bolton, K. Molecular Dynamics Study of the Catalyst Particle Size Dependence on Carbon Nanotube Growth. *J. Chem. Phys.* **2004**, *121*, 2775–2779.
19. Ding, F.; Rosén, A.; Bolton, K. The Role of the Catalytic Particle Temperature Gradient for SWNT Growth from Small Particles. *Chem. Phys. Lett.* **2004**, *393*, 309–313.
20. Ding, F.; Bolton, K.; Rosén, A. Structure and Thermal Properties of Supported Catalyst Clusters for Single-Walled Carbon Nanotube Growth. *Appl. Surf. Sci.* **2006**, *252*, 5254–5258.
21. Zhao, J.; Martinez-Limia, A.; Balbuena, P. B. Understanding Catalyzed Growth of Single-Wall Carbon Nanotubes. *Nanotechnology* **2005**, *16*, S575–S581.
22. Ribas, M. A.; Ding, F.; Balbuena, P. B.; Yakobson, B. I. Nanotube Nucleation *versus* Carbon-Catalyst Adhesion-Probed by Molecular Dynamics Simulations. *J. Chem. Phys.* **2009**, *131*, 224501.
23. Burgos, J. C.; Reyna, H.; Yakobson, B. I.; Balbuena, P. B. Interplay of Catalyst Size and Metal-Carbon Interactions on the Growth of Single-Walled Carbon Nanotubes. *J. Phys. Chem. C* **2010**, *114*, 6952.
24. Raty, J.-Y.; Gygi, F.; Galli, G. Growth of Carbon Nanotubes on Metal Nanoparticles: A Microscopic Mechanism from *ab Initio* Molecular Dynamics Simulations. *Phys. Rev. Lett.* **2005**, *95*, 096103.
25. Amara, H.; Bichara, C.; Ducastelle, F. Understanding the Nucleation Mechanisms of Carbon Nanotubes in Catalytic Chemical Vapor Deposition. *Phys. Rev. Lett.* **2008**, *100*, 056105.
26. Ohta, Y.; Okamoto, Y.; Page, A. J.; Irle, S.; Morokuma, K. Quantum Chemical Molecular Dynamics Simulation of Single-Walled Carbon Nanotube Cap Nucleation on an Iron Particle. *ACS Nano* **2009**, *3*, 3413–3420.
27. Page, A. J.; Irle, S.; Morokuma, K. Polyyne Chain Growth and Ring Collapse Drives Ni-Catalyzed SWNT Growth: A QM/MD Investigation. *J. Phys. Chem. C* **2010**, *114*, 8206–8211.
28. Yao, Y.; Liu, R.; Zhang, J.; Jiao, L. Y.; Liu, Z. F. Raman Spectral Measuring of the Growth Rate of Individual Single-Walled Carbon Nanotubes. *J. Phys. Chem. C* **2007**, *111*, 8407–8409.
29. Voter, A. F.; Montalenti, F.; Germann, T. C. Extending the Time Scale in Atomistic Simulation of Materials. *Ann. Rev. Mater. Res.* **2002**, *32*, 321–346.

30. Neyts, E.; Shibuta, Y.; Bogaerts, A. Bond Switching Regimes in Nickel and Nickel−Carbon Nanoclusters. *Chem. Phys. Lett.* **2010**, *488*, 202–205.

31. Dereli, G. Stillinger-Weber Type Potentials in Monte-Carlo Simulation of Amorphous Silicon. *Mol. Simul.* **1992**, *8*, 351–360.

32. Timonova, M.; Groenewegen, J.; Thijsse, B. J. Modeling Diffusion and Phase Transitions by a Uniform-Acceptance Force-Bias Monte Carlo Method. *Phys. Rev. B* **2010**, *81*, 144107.

33. Neyts, E. C.; Bogaerts, A. Numerical Study of the Size-Dependent Melting Mechanisms of Nickel Nanoclusters. *J. Phys. Chem. C* **2009**, *113*, 2771–2776.

34. Zhao, Q.; Nardelli, M. B.; Bernholc, J. Ultimate Strength of Carbon Nanotubes: A Theoretical Study. *Phys. Rev. B* **2002**, *65*, 144105.

35. Zhang, P.; Lammert, P. E.; Crespi, V. H. Plastic Deformations of Carbon Nanotubes. *Phys. Rev. Lett.* **1998**, *81*, 5346–5349.

36. Balbuena, P. B.; Seminario, J. M. In *Nanomaterials: Design and Simulation*; Elsevier: Amsterdam, The Netherlands, 2007.

37. Nielson, K. D.; van Duin, A. C. T.; Oxgaard, J.; Deng, W.-Q.; Goddard, W. A., III. Development of the ReaxFF Reactive Force Field for Describing Transition Metal Catalyzed Reactions, with Application to the Initial Stages of the Catalytic Formation of Carbon Nanotubes. *J. Phys. Chem. A* **2005**, *109*, 493–499.

38. van Duin, A. C. T.; Dasgupta, S.; Lorant, F.; Goddard, W. A., III. ReaxFF: A Reactive Force Field for Hydrocarbons. *J. Phys. Chem. A* **2001**, *105*, 9396–9409.

39. Mueller, J. E.; van Duin, A. C. T.; Goddard, W. A., III. Development and Validation of ReaxFF Reactive Force Field for Hydrocarbon Chemistry Catalyzed by Nickel. *J. Phys. Chem. C* **2010**, *114*, 5675.

40. Abell, G. C. Empirical Chemical Pseudopotential Theory of Molecular and Metallic Bonding. *Phys. Rev. B* **1985**, *31*, 6184–6196.

41. Tersoff, J. Empirical Interatomic Potential for Carbon, with Applications to Amorphous Carbon. *Phys. Rev. Lett.* **1988**, *61*, 2879–2882.

42. Brenner, D. W. Empirical Potential for Hydrocarbons for Use in Simulating the Chemical Vapor-Deposition of Diamond Films. *Phys. Rev. B* **1990**, *42*, 9458–9471.

43. Mortier, W. J.; Ghosh, S. K.; Shankar, S. Electronegativity Equalization Method for the Calculation of Atomic Charges in Molecules. *J. Am. Chem. Soc.* **1986**, *108*, 4315–4320.

44. van Duin, A. C. T.; Baas, J. M. A.; van de Graaf, B. Delft Molecular Mechanics−A New Approach to Hydrocarbon Force-Fields−Inclusion of a Geometry-Dependent Charge Calculation. *J. Chem. Soc., Faraday Trans.* **1994**, *90*, 2881–2895.

45. Buehler, M. J.; Tang, H.; van Duin, A. C. T.; Goddard III, W. A. Threshold Crack Speed Controls Dynamical Fracture of Silicon Single Crystals. *Phys. Rev. Lett.* **2007**, *99*, 165502.

46. Garcia, A. P.; Buehler, M. J. Bioinspired Nanoporous Silicon Provides Great Toughness at Great Deformability. *Comput. Mater. Sci.* **2010**, *48*, 303–309.

47. Nakano, A.; Kalia, R. K.; Nomura, K.; Sharma, A.; Vashishta, P.; Shimojo, F.; van Duin, A. C. T.; Goddard, W. A.; Biswas, R.; Srivastava, D. A Divide-and-Conquer/Cellular-Decomposition Framework for Million-to-Billion Atom Simulations of Chemical Reactions. *Comput. Mater. Sci.* **2007**, *38*, 642–652.

48. Zybin, S. V.; Goddard III, W. A.; Xu, P.; van Duin, A. C. T.; Thompson, A. P. Physical Mechanism of Anisotropic Sensitivity in Pentaerythritol Tetranitrate from Compressive-Shear Reaction Dynamics Simulations. *Appl. Phys. Lett.* **2010**, *96*, 081918.